Journal of Engineering Mathematics **34:** 143–162, 1998.

Boundary-integral-equation methods for screen problems in acoustic and electromagnetic aerospace research

H. SCHIPPERS
National Aerospace Laboratory NLR, P.O. Box 90502, 1006 BM Amsterdam,The Netherlands

Received 1 August 1997; accepted in revised form 5 December 1997

Abstract. The paper describes the application of boundary-integral-equation methods to solve two problems in acoustic and electromagnetic aerospace research. The first problem is concerned with the structural-acoustic analysis of solar arrays of satellites. This analysis involves the solution of a boundary-integral equation for determining the acoustic pressure jump across the solar panels. The solar panels are geometrically modelled as screens (*i.e.* open surfaces in three-dimensional space). The second problem is related to the radar cross section prediction of engine inlets of fighter aircraft. The prediction requires the calculation of the scattered electromagnetic field when the inlet is illuminated by a radar beam. Engine inlets are modelled as three-dimensional perfectly conducting cavity-like screens. The scattered electric field is obtained by the numerical solution of the Electric-Field Integral Equation.

Keywords: boundary-integral equations, acoustics, electromagnetics, screens, solar panels, radar signature, scattering.

1. Introduction

In aerospace research, boundary-integral-equation methods are frequently used in various fields of applied mechanics for solving problems around thin obstacles. Geometrically, these thin obstacles are modelled as screens, *i.e.* open surfaces in three-dimensional space. Since about 1950 many investigations have been performed to analyse the aerodynamic flow about (parts of) aircraft. In particular, lifting-surface theory has been applied extensively to predict lift distributions on wings and propeller blades. Appropriate boundary-integral equations were derived, and suitable numerical methods to solve these equations were developed.

Before the advent of the digital computer, boundary-integral equations were solved by means of basis functions with support on the whole boundary. Such global basis functions were advantageous from the point of view that the number of unknown coefficients was limited, so that the equations could be solved by the computational tools which were available at that time. In 1950 an important method for predicting the lift distribution on wings in the subsonic speed regime was presented by Multhopp [1]. In this method the wing is approximated by a plane sheet extending over the wing-platform. The mathematical problem is formulated in terms of an integral equation which relates the prescribed normal velocity on the wing surface with the pressure distribution over the wing surface. The pressure distribution is approximated by trigonometric basis functions satisfying the correct behaviour at the leading and trailing edges. The coefficients of the basis functions are determined by means of a collocation method. When digital computers became available, the convergence of this method was investigated by Zandbergen *et al.* in the 1960's. Lack of convergence was observed due to poor modelling of the singular behaviour of the kernel function. The method

was improved by Zandbergen *et al.* in [2]. Also, the range of applicability was extended to kinked wings [3]. The extension of this method to complex aircraft configurations (*e.g.* configurations with extended slats and flaps consisting of several segments) is, however, far from trivial, because the global basis functions are defined on a single, simply connected domain that can be mapped onto a simple rectangular sheet. Instead, numerical methods were developed that use basis functions with local support. These so-called panel methods appear to be more tractable for treating complex geometries. Since the mid 1960's panel methods have been developed to the extent that they are routinely being used in the aerospace industry.

The major drawback of boundary-integral-equation methods in aerodynamics is that their range of applicability is restricted to linear inviscid potential flow, *i.e.* nonlinear compressibility effects cannot be taken into account. As a consequence, transonic flows with shock waves cannot be treated by boundary-integral-equation methods. Therefore, from one of the major fields in aerospace research, *viz.* the analysis of aerodynamic flow around aircraft, there seem to be no pushing factors for further development of boundary-integral-equation methods. Instead, since about the mid 70's the investigations in this field have been addressed to the development of computational methods for the solution of nonlinear flows governed by the full-potential equation, Euler equations and Navier-Stokes equations. However, new challenges have appeared for the development and application of boundary-integral-equation methods in other fields of aerospace research. In the present paper the following problems are discussed:

Structural-acoustic analysis of solar arrays on satellites
Modern spacecraft are equipped with large light-weight solar arrays. A solar array consists of a stack of solar panels, which is unfolded in orbit flight. During the launching phase the solar panels are folded into small packages and the distance between the panels is small. Then the solar array is exposed to severe dynamic loads which may affect the dynamic behaviour of the satellite. Therefore, it is a prerequisite to analyse the dynamic behaviour of the solar arrays in interaction with the main structure of the satellite and to assess the effects of the vibrating air. The coupled structural-acoustic analysis of the solar array and the surrounding air involves the solution of a hyper-singular integral equation for determining the acoustic pressure jump across the solar panels. The panels are geometrically modelled as screens. The hyper-singular integral equation is numerically solved by a boundary-element method, where the acoustic pressure jump is approximated by piecewise linear functions on a triangular surface grid.

Radar-Cross-Section (RCS) calculations
The development of prediction techniques for radar cross sections of aerospace platforms is motivated by the need to have tools available for both radar analysis and design of military aerospace vehicles. The vulnerability of fighter aircraft in several types of missions is among others determined by their detectability by radar systems of which the frequency can vary typically from 0·1 to 94 GHz, corresponding with wavelengths of 3 meters to 3 millimeters. RCS predictions of aerospace platforms require the calculation of the fields scattered by the platform when illuminated by a plane electromagnetic wave (the radar beam). When illuminated nose-on, the engine inlets of aircraft account for approximately 90 % of the radar signature due to multiple reflections in these inlets. The interior surface of engine inlets is modelled as a three-dimensional perfectly conducting cavity-like screen. Then, the scattered electric field is obtained from the numerical solution of the Electric-Field Integral Equation

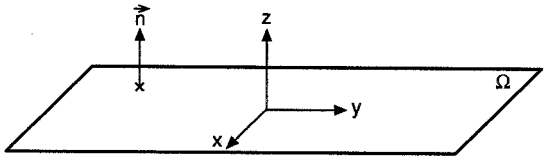

Figure 1. Solar panel with coordinate system.

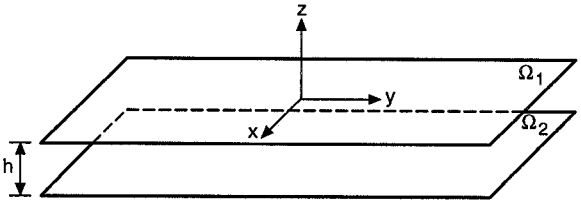

Figure 2. Two parallel solar panels at a small distance h apart from each other.

(EFIE). The method of moments is applied to solve this equation. In this method the local basis functions are defined by the classical Glisson-Rao vector functions on a triangular surface grid.

2. Structural-acoustic analysis of solar arrays

On earth the dynamic behaviour of solar arrays is investigated by ground vibration tests. The results of these tests are verified by performing modal analysis using a finite-element model in vacuum, *i.e.* the effects of the surrounding air in the test environment are neglected. When the results of the ground vibration tests and the modal analysis are compared, deviations of more than 10 % are observed with regard to the eigenfrequencies. In this section a computational model is described to estimate the acoustic effect of the surrounding air on the harmonic vibration of a single solar panel (see Figure 1) and an array of two parallel solar panels in close proximity (see Figure 2). The analysis involves the solution of a hypersingular integral equation. For low frequencies, it will be shown that the vibrating air behaves as a virtual mass which can be added to the mass of the panel. For the case of two parallel solar panels in close proximity, a structural-acoustic analysis is presented which is based on the modal analysis of a single solar panel. The acoustic energy of the vibrating air on the panels is estimated in terms of the small distance h between the two panels. The consequences of these energy estimates on the values of the lowest eigenfrequencies of two vibrating panels are discussed.

2.1. Mathematical formulation

The solar panels are modelled as screens, *i.e.* smooth open surfaces in $\mathbf{R}^3$. The structural analysis is based on the Reissner-Mindlin theory for moderately thick plates. This theory assumes that the in plane displacements w_1 and w_2 have the form

$$w_1(x, y, z) = z\beta_1(x, y), \quad w_2(x, y, z) = z\beta_2(x, y) \tag{1}$$

and that the normal displacement w_3 has the form

$$w_3(x, y, z) = w(x, y). \tag{2}$$

The dynamics of a single harmonically vibrating panel is governed by the weak formulation: find a displacement field $\mathbf{w} = (w_1, w_2, w_3)^T$ of the form (1) – (2) such that

$$K(\mathbf{v}, \mathbf{w}) - \rho\omega^2 M(\mathbf{v}, \mathbf{w}) = (\mathbf{n} \cdot \mathbf{v}, \mu) \tag{3}$$

for all possible virtual displacement fields $\mathbf{v}$ of form (1) – (2). Here, $K(\mathbf{v}, \mathbf{w})$ and $M(\mathbf{v}, \mathbf{w})$ denote, respectively, the first variation of the strain energy and the kinetic energy, which are given in [4]. Furthermore, ρ denotes the density of the solar panels and ω the angular frequency. The right-hand side of (3) represents the acoustic work over the virtual normal displacement $\mathbf{n} \cdot \mathbf{v}$ by the acoustic pressure jump

$$\mu = p^+ - p^-, \tag{4}$$

with p^+ (p^-) denoting the pressure on the upper (lower) side of the solar panel. Hence,

$$(\mathbf{n} \cdot \mathbf{v}, \mu) = \int_\Omega \mathbf{n} \cdot \mathbf{v}\, \mu \, \mathrm{d}S, \tag{5}$$

where Ω is the domain of the plate. When the solar array consists of multiple panels, Equation (3) holds for each panel.

First consider the single solar panel (Figure 1). If the panel vibrates in vacuum, then $\mu = 0$. In this case (3) corresponds with a classical eigenvalue problem. The solution of this problem yields the vibration modes and the eigenfrequencies of the panel in vacuum. However, if the panel vibrates in air, the pressure jump μ does not in general vanish. Below, an expression for μ in terms of $w_n = \mathbf{n} \cdot \mathbf{w}$ is derived, which changes (3) into a perturbed eigenvalue problem. The acoustics are governed by the Helmholtz equation. The sound pressure of the vibrating air satisfies the following boundary-integral formula

$$p(\mathbf{r}) = -\int_\Omega \frac{\partial G}{\partial n'}(\mathbf{r}, \mathbf{r}')\mu(\mathbf{r}')\, \mathrm{d}S', \qquad \mathbf{r} \in \mathbf{R}^3 \setminus \Omega, \tag{6}$$

where G represents the fundamental solution of the Helmholtz equation in an infinite domain,

$$G(\mathbf{r}, \mathbf{r}') = \frac{\mathrm{e}^{-jk|\mathbf{r}-\mathbf{r}'|}}{4\pi|\mathbf{r} - \mathbf{r}'|}, \quad \forall \mathbf{r} \neq \mathbf{r}', \tag{7}$$

with k the wave number ($k = \omega/c$ with c the speed of sound).

The vibrating panel and the vibrating air are coupled by the acoustic coupling equation

$$\frac{\partial p}{\partial n} = \rho_a \omega^2 w_n, \tag{8}$$

where ρ_a is the density of the air. Application of this boundary condition to the boundary-integral formula (6) yields the hypersingular integral equation

$$-\int_\Omega \frac{\partial^2 G}{\partial n \partial n'}(\mathbf{r}, \mathbf{r}')\mu(\mathbf{r}')\, \mathrm{d}S' = \rho_a \omega^2 w_n(\mathbf{r}), \quad \mathbf{r} \in \Omega, \tag{9}$$

or in operator notation:

$$T\mu = \rho_a \omega^2 w_n. \tag{10}$$

In Equation (9), the integral $\neq$ is defined as a finite-part integral in the sense of Hadamard. The mathematical aspects of the integral equation (9), as defined on screens in $\mathbf{R}^3$, have been studied in detail by Stephan [5]. In that paper it has been proved that the operator T defines a continuous mapping from $\tilde{H}^s(\Omega)$ onto $H^{s-1}(\Omega)$ for any real number s. Here $\tilde{H}^s(\Omega)$ is defined as in [5]: if V is a bounded domain with smooth boundary Γ and $\Omega \subset \Gamma$, then $\tilde{H}^s(\Omega) = \{u \in H^s(\Gamma) : \text{supp } u \subset \Omega\}$. The inverse of the operator T exists as a continuous mapping from $H^{-1/2}(\Omega)$ onto $\tilde{H}^{1/2}(\Omega)$, (see [5], theorem 2.7), so that (10) yields the following expression for the pressure jump in terms of w_n

$$\mu = \rho_a \omega^2 T^{-1} w_n. \tag{11}$$

When this expression is substituted in (3) the following coupled differential boundary-integral equation is obtained

$$K(\mathbf{v}, \mathbf{w}) - \rho\omega^2 M(\mathbf{v}, \mathbf{w}) - \rho\epsilon\ \omega^2 (v_n, T^{-1} w_n) = 0, \quad \epsilon = \frac{\rho_a}{\rho}. \tag{12}$$

Note that ϵ has no physical dimension. For metallic plates ϵ is so small that the last term in (12) may be neglected in the structural-acoustic analysis. For solar panels, however, ϵ is of the order of 0·01, and it will be shown in this paper that then the vibrating air does have a nonnegligible effect on the values of the eigenfrequencies.

Equation (12) defines a compactly perturbed eigenvalue problem. The problem depends in a non linear way on ω^2, due to the implicit occurrence of ω in T through the Green function G via $k = \omega/c$. Equation (12) can be solved by means of an iteration process for each eigenfrequency: solve for $i = 1, 2, 3, \ldots$

$$K(\mathbf{v}, \mathbf{w}_i) - \rho\omega_i^2 M(\mathbf{v}, \mathbf{w}_i) - \rho\epsilon\ \omega_i^2 (v_n, T_{\omega_{i-1}}^{-1} w_{n,i}) = 0. \tag{13}$$

The dependence of T on ω is stressed by the notation T_ω. Initial values for the eigenmodes and eigenfrequencies are obtained from the solution of (12) in vacuum where $\epsilon = 0$. The eigenfrequencies in vacuum are used to evaluate T_{ω_0}. The convergence of this iteration process has been investigated in [6].

The numerical calculations are based on the simultaneous solution of differential equation (3) and boundary-integral equation (10) in terms of the following weak formulation: find nontrivial $\mathbf{w} \in (H^1(\Omega))^3$, $\mu \in \tilde{H}^{1/2}(\Omega)$ and $\omega \in \mathbf{R}^1$ such that

$$K(\mathbf{v}, \mathbf{w}) - \rho\omega^2 M(\mathbf{v}, \mathbf{w}) - (\mathbf{n} \cdot \mathbf{v}, \mu) = 0, \tag{14}$$

$$-(\xi, \mathbf{n} \cdot \mathbf{w}) + \frac{1}{\rho_a \omega^2} (\xi, T\mu) = 0, \tag{15}$$

for all $\mathbf{v} \in (H^1(\Omega))^3$, $\xi \in \tilde{H}^{1/2}(\Omega)$. The bilinear form $(\xi, T\mu)$ in (15) reads

$$(\xi, T\mu) = -\int_\Omega \oint_\Omega \frac{\partial^2 G}{\partial n \partial n'}(\mathbf{r}, \mathbf{r}')\nu(\mathbf{r}')\xi(\mathbf{r})\, \mathrm{d}S'\, \mathrm{d}S. \tag{16}$$

Equation (14) is discretized by finite elements and Equation (15) by boundary elements.

The hypersingular integral operator is regularised through integration by parts. In view of the fact that μ and ξ vanish along the edges of the plates (*i.e.* no pressure jump along $\partial\Omega$) and

that G is the fundamental solution of the Helmholtz operator, the following expression can be derived for $(\xi, T\mu)$ (see also [7]),

$$(\xi, T\mu) = \int_\Omega \int_\Omega G(\mathbf{r}, \mathbf{r}\,') \langle \mathbf{n}_r \times \nabla_r \xi(\mathbf{r}), \mathbf{n}_{r'} \times \nabla_{r'} \mu(\mathbf{r}\,') \rangle \, \mathrm{d}S\,' \, \mathrm{d}S$$
$$-k^2 \int_\Omega \int_\Omega G(\mathbf{r}, \mathbf{r}\,') \, \mu(\mathbf{r}\,') \, \xi(\mathbf{r}) \, \langle \mathbf{n}_r, \mathbf{n}_{r'} \rangle \, \mathrm{d}S\,' \, \mathrm{d}S, \tag{17}$$

where $\langle \mathbf{a}, \mathbf{b} \rangle$ denotes the inner product of $\mathbf{a}$ and $\mathbf{b}$. Note that (17) contains only weakly singular integrals.

2.2. Low-frequency analysis

For low frequencies, the Green function G can be approximated by

$$G(\mathbf{r}, \mathbf{r}\,') = \frac{1}{4\pi |\mathbf{r} - \mathbf{r}\,'|} - \frac{jk}{4\pi} + \mathcal{O}(k^2). \tag{18}$$

When this approximation is substituted in Equation (17), it follows that

$$(\xi, T\mu) = \int_\Omega \int_\Omega \frac{1}{4\pi |\mathbf{r} - \mathbf{r}\,'|} \langle \mathbf{n}_r \times \nabla_r \xi(\mathbf{r}), \mathbf{n}_{r'} \times \nabla_{r'} \mu(\mathbf{r}\,') \rangle \, \mathrm{d}S\,' \, \mathrm{d}S$$
$$-\frac{jk}{4\pi} \int_\Omega \int_\Omega \langle \mathbf{n}_r \times \nabla_r \xi(\mathbf{r}), \mathbf{n}_{r'} \times \nabla_{r'} \mu(\mathbf{r}\,') \rangle \, \mathrm{d}S\,' \, \mathrm{d}S + \mathcal{O}(k^2). \tag{19}$$

Similarly, the operator T may be approximated by (compare (9) and (10))

$$T = T_0 - jkD_0 + \mathcal{O}(k^2), \tag{20}$$

where T_0 and D_0 are defined by the bilinear forms in the right hand side of (19). It can be proved that the operator T_0 is positive definite on $\tilde{H}^{1/2}(\Omega)$. The inverse of this approximation for T reads

$$T^{-1} = T_0^{-1} + jkT_0^{-1} D_0 T_0^{-1} + \mathcal{O}(k^2), \tag{21}$$

so that Equation (12) can be approximated up to third order in ω by

$$K(\mathbf{v}, \mathbf{w}) - \rho\omega^2 M(\mathbf{v}, \mathbf{w}) - \rho\epsilon \, \omega^2 (\mathbf{n} \cdot \mathbf{v}, T_0^{-1} \mathbf{n} \cdot \mathbf{w})$$
$$+(j\omega)^3 \, \frac{\rho\epsilon}{c} \, (\mathbf{n} \cdot \mathbf{v}, T_0^{-1} D_0 T_0^{-1} \mathbf{n} \cdot \mathbf{w}) = 0. \tag{22}$$

Note that the first term of (21) can be seen as a virtual mass (of the vibrating air), which is added to the mass of the solar panel. The second term of (21) induces the last term in Equation (22), which is proportional to ω^3. For low frequencies the contribution of this term to the perturbation of the eigenfrequencies is small.

2.3. Two parallel solar panels

For the case of two parallel solar panels (modelled as two rectangular plates Ω_1 and Ω_2), at a small distance h apart from each other (see Figure 2), the mathematical formulation is adjusted

when Ω is defined as $\Omega = \Omega_1 \cup \Omega_2$. The acoustic coupling Equation (8) is applied to both plates Ω_1 and Ω_2, so that the following system of boundary-integral equations is obtained,

$$\begin{aligned} T_{11}\mu_1 + T_{12}\mu_2 &= \rho_a \omega^2 \, \mathbf{n} \cdot \mathbf{w}_1, \quad \text{on } \Omega_1, \\ T_{21}\mu_1 + T_{22}\mu_2 &= \rho_a \omega^2 \, \mathbf{n} \cdot \mathbf{w}_2, \quad \text{on } \Omega_2, \end{aligned} \tag{23}$$

where μ_i and $\mathbf{w}_i$ $(i = 1, 2)$ denote the jump in the acoustic pressure and the displacement field on Ω_i, respectively. The boundary-integral operators T_{ij} are given by

$$T_{ij}\mu_j(\mathbf{r}) = -\int\!\!\!\!\!\!-_{\Omega_j} \frac{\partial^2 G}{\partial n \partial n'}(\mathbf{r}, \mathbf{r}')\mu_j(\mathbf{r}') \, \mathrm{d}S', \quad \mathbf{r} \in \Omega_i. \tag{24}$$

Observe that the integral operators T_{11} and T_{22} correspond to the operator T of (10). Hence

$$T_{11} = T_{22} = T. \tag{25}$$

The operators T_{12} and T_{21} model the acoustic effects that the plates have upon each other. The weak formulation (15) is used for the solution of (23). The bilinear form related to T_{12} is, see (17),

$$(\xi_1, T_{12}\mu_2) = \int_{\Omega_1}\int_{\Omega_2} G(\mathbf{r}, \mathbf{r}') \{\langle \mathbf{n} \times \nabla\xi_1, \mathbf{n}' \times \nabla'\mu_2\rangle - k^2 \xi_1 \mu_2 \langle \mathbf{n}, \mathbf{n}'\rangle\} \, \mathrm{d}S' \, \mathrm{d}S. \tag{26}$$

These integrals are of regular type, but their evaluation by means of numerical integration rules has to be carried out carefully, because the Green function G behaves as $1/h$ if $|\mathbf{r} - \mathbf{r}'|$ is small (*i.e.* when $\mathbf{r}$ and $\mathbf{r}'$ are opposite to each other). Appropriate quadrature formulas have been presented in [8]. Obviously, the above formulation can be extended to a solar array consisting of an arbitrary number of panels.

2.4. Estimates of acoustic energy

For a single vibrating panel the acoustic energy of the vibrating air on a solar panel is proportional to

$$\mathcal{A}_1 = \int_\Omega \mathbf{n} \cdot \mathbf{w} \, \mu \, \mathrm{d}S, \quad \text{with} \quad \mu = \rho_a \omega^2 \, T^{-1} \, \mathbf{n} \cdot \mathbf{w}. \tag{27}$$

Similarly, for two vibrating panels the acoustic energy is related to

$$\mathcal{A}_2 = \int_{\Omega_1 \cup \Omega_2} \mathbf{W} \cdot \boldsymbol{\mu} \, \mathrm{d}S, \tag{28}$$

with

$$\mathbf{W} = \begin{pmatrix} \mathbf{n} \cdot \mathbf{w}_1 \\ \mathbf{n} \cdot \mathbf{w}_2 \end{pmatrix} \quad \text{and} \quad \boldsymbol{\mu} = \rho_a \omega^2 Z^{-1} \mathbf{W}, \tag{29}$$

where Z corresponds to the matrix of operators on the left-hand side of Equation (23),

$$Z = \begin{pmatrix} T_{11} & T_{12} \\ T_{21} & T_{22} \end{pmatrix}. \tag{30}$$

When the distance between the panels is large, there is no interaction between the panels ($T_{12} = T_{21} = 0$ in Equation (23)). Then, $\mu_1 = \rho_a \omega^2\, T^{-1}\, \mathbf{n} \cdot \mathbf{w}_1$ and $\mu_2 = \rho_a \omega^2\, T^{-1}\, \mathbf{n} \cdot \mathbf{w}_2$. As a consequence, the acoustic energy corresponds to the energy of two single solar panels, *i.e.*

$$\mathcal{A}_2 = \rho_a \omega^2 \left(\int_{\Omega_1} \mathbf{n} \cdot \mathbf{w}_1 T^{-1} \mathbf{n} \cdot \mathbf{w}_1 \, \mathrm{d}S + \int_{\Omega_2} \mathbf{n} \cdot \mathbf{w}_2 T^{-1} \mathbf{n} \cdot \mathbf{w}_2 \, \mathrm{d}S \right). \tag{31}$$

For panels in close proximity, a first-order expansion of T_{12} in terms of h has been derived in [9]. It was shown that T_{12} may be approximated up to first order in h by

$$T_{12} = T - \tfrac{1}{2} h V, \tag{32}$$

where the operator V is related to the weak formulation of the Helmholtz equation, *i.e.* ,

$$(\xi, V\mu) = \int_{\Omega_1} (\nabla_s \mu \cdot \nabla_s \xi - k^2 \xi \mu) \, \mathrm{d}S, \tag{33}$$

with $\xi = \mu = 0$ on the edge of Ω_1. A similar relation holds for T_{21}. Equations (23), (25) and (32) can now be used to estimate the acoustic effects of in-phase vibration of the panels (given by $\mathbf{w}_1 = \mathbf{w}_2 = \mathbf{w}$) and out-of-phase vibration (given by $\mathbf{w}_1 = -\mathbf{w}_2 = \mathbf{w}$).

If the panels are vibrating in-phase, the pressure jumps over the panels is given by

$$\mu_1 = \mu_2 = \tfrac{1}{2} \rho_a \omega^2 (T^{-1} + \tfrac{1}{4} h T^{-1} V T^{-1})\, \mathbf{n} \cdot \mathbf{w}. \tag{34}$$

Then, the acoustic energy $\mathcal{A}_2$ becomes for small values of h, compare (27),

$$\begin{aligned} \mathcal{A}_2 \;&=\; \rho_a \omega^2 \left(\int_{\Omega_1} \mathbf{n} \cdot \mathbf{w}\, T^{-1}\, \mathbf{n} \cdot \mathbf{w} \, \mathrm{d}S + \frac{1}{4} h \int_{\Omega_1} \mathbf{n} \cdot \mathbf{w}\, T^{-1} V T^{-1}\, \mathbf{n} \cdot \mathbf{w} \, \mathrm{d}S \right) \\ &=\; \mathcal{A}_1 + O(h). \end{aligned} \tag{35}$$

Comparison of this expression with (31) shows that, when the distance h between the panels tends to zero, the acoustic energy tends to half the value for two single solar panels (without interaction). For small values of h, the acoustic energy of two in-phase vibrating panels thus corresponds to the acoustic energy of a single solar panel with air on both sides, but with half the value of the air density.

When the panels are vibrating out-of-phase, it follows from (23), (25) and (32) that

$$\mu_1 = -\mu_2 = \rho_a \omega^2 \frac{2}{h} V^{-1} \mathbf{n} \cdot \mathbf{w}. \tag{36}$$

Then, the acoustic energy $\mathcal{A}_2$ becomes for small values of h,

$$\mathcal{A}_2 = \rho_a \omega^2 \frac{4}{h} \int_{\Omega_1} \mathbf{n} \cdot \mathbf{w}\, V^{-1}\, \mathbf{n} \cdot \mathbf{w} \, \mathrm{d}S, \tag{37}$$

which is completely different from the relation (35) for in-phase vibrating panels. Now the acoustic effects are dominated by the vibrating air between the panels, and the acoustic energy is inversely proportional to the distance h. When the panels vibrate out-of-phase, the air is pumped in and out of the gap between the panels, which causes a large energy transfer from

the panels to the air in the gap. So far it has been assumed that the air could be treated as inviscid. For narrow gaps, however, the viscosity of the air cannot be neglected for out-of-phase vibration. A more sophisticated model (including effects of inertia, viscosity, compressibility and thermal conductivity) has been presented in [10]. It is shown there that the viscosity of the air results in a significant amount of damping when the distance between the panels is small.

2.5. NUMERICAL SOLUTION

The cross-sectional rotations β_1, β_2 and the normal displacement w in Equations (1) – (2) are approximated by the four-noded C^0 elements of [11]. This finite-element approximation of Equation (14) yields the following system of algebraic equations

$$(\mathcal{K} - \omega^2 \mathcal{M})\mathbf{U} = \mathbf{F}_a. \tag{38}$$

The matrices $\mathcal{K}$ and $\mathcal{M}$ are the stiffness and mass matrix of the solar array, respectively. The vector $\mathbf{U}$ contains the nodal displacements. The load vector $\mathbf{F}_a$, due to the pressure jump μ, is given by

$$\mathbf{F}_a = \mathcal{C}^T \mathbf{J}, \tag{39}$$

in which $\mathcal{C}$ is the matrix which couples the displacement degrees of freedom with the pressure jump degrees of freedom. The vector $\mathbf{J}$ contains the nodal pressure jumps.

The boundary-integral equation (15) is solved by a boundary-element method on a triangular surface grid of which the nodes correspond to the nodes of the quadrilateral mesh of the structural four-noded C^0 elements. The computational aspects of this boundary-element method have been described in [8], where special attention has been given to the evaluation of singular and nearly singular integrals. For (15) the discrete system of equations becomes

$$\mathcal{T}\mathbf{J} = \rho_a \, \omega^2 \, \mathcal{C} \, \mathbf{U}. \tag{40}$$

Substitution of (40) in Equations (38) and (39) yields

$$(\mathcal{K} - \rho\omega^2(\mathcal{M} + \mathcal{M}_a))\mathbf{U} = 0, \tag{41}$$

with $\mathcal{M}_a = \epsilon \, \mathcal{C}^T \mathcal{T}^{-1} \mathcal{C}$. For low frequencies the matrix $\mathcal{M}_a$ can be approximated by (compare Equation (22)),

$$\mathcal{M}_a = \epsilon \, \mathcal{C}^T \mathcal{T}_0^{-1} \mathcal{C} - j\omega \frac{\epsilon}{c} \mathcal{C}^T \mathcal{T}_0^{-1} \mathcal{D}_0 \mathcal{T}_0^{-1} \mathcal{C}. \tag{42}$$

When the second term of (42) is neglected, the lowest eigenfrequency of Equation (41) reads

$$\omega^2 = \frac{\langle \mathcal{K}\mathbf{U}_1, \mathbf{U}_1 \rangle}{\langle \mathcal{M}\mathbf{U}_1, \mathbf{U}_1 \rangle + \langle \mathcal{M}_{a,0}\mathbf{U}_1, \mathbf{U}_1 \rangle}, \tag{43}$$

where $\mathbf{U}_1$ is the eigenmode corresponding to the lowest eigenfrequency and $\mathcal{M}_{a,0}$ represents the first term of (42). By the bijectivity of T_0 and its positive definiteness, it follows that $\langle \mathcal{M}_{a,0}\mathbf{U}_1, \mathbf{U}_1 \rangle > 0$. From (43) it follows that the lowest eigenfrequency of the problem in air (41) will be smaller than the corresponding eigenfrequency of the problem in vacuum.

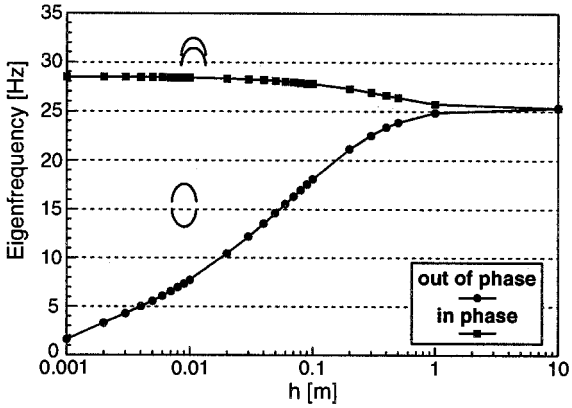

Figure 3. Two parallel panels: influence panel distance h on the eigenfrequencies of the first (pair of) eigenmodes.

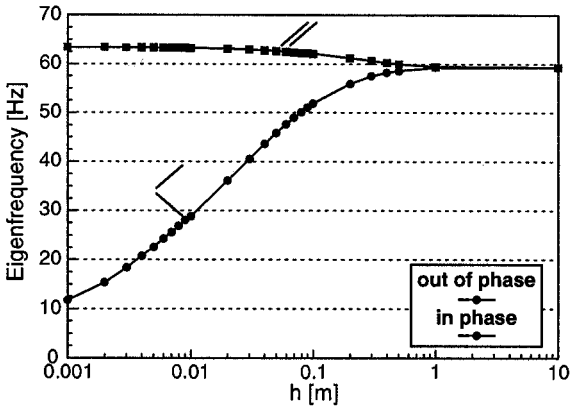

Figure 4. Two parallel panels: influence panel distance h on the eigenfrequencies of the second (pair of) eigenmodes.

2.6. APPLICATIONS

The computational model of the previous section has been applied to representative flat solar-array panels. The solar panels are sandwich panels with different core and fairing properties. For the analysis the panels are modelled as monolithic plates having the same mass per unit area and bending stiffness. The basic properties of the panels are: length 1·675 m, width 1·25 m, thickness 0·001 m, elasticity modulus 4·5444 E^{+13} N/m^2, Poisson's ratio 0·3, density ρ = 1122·2 kg/m^3. The panels are simply supported along the short edges. The large edges are free. The computational mesh on a single panel consists of 16×16 quadrilateral elements. The triangular grid for the numerical solution of Equation (15) is obtained by the subdivision of each quadrilateral element into two parts. The density and the speed of sound of the surrounding air are ρ_a = 1·2 kg/m^3 and c = 340 m/s.

For a single solar panel (with the above properties) the eigenfrequencies of the first five eigenmodes are given in Table 1. The in-air eigenfrequencies are computed by means of the iterative procedure discussed with Equation (13). When the in-vacuum and in-air frequencies are compared, it is observed that the air has a large influence on the dynamic behaviour of a single panel. The eigenfrequencies are shifted downwards significantly, as could be expected, since the panel experiences the air as an added mass (see Equation (43)).

Table 1. Eigenfrequencies (in Hz) of a single panel in vacuum and in air

mode	1	2	3	4	5
in-vacuum	33·25	68·58	136·67	182·31	192·25
in-air	25·30	59·14	110·21	158·02	166·98

For two solar panels in close proximity (see Figure 2), Figures 3 and 4 display the eigenfrequencies of the first and second pair of eigenmodes. A pair of eigenmodes consists of the two cases where the panels vibrate in-phase and out-of-phase, in each case with the same eigenmode per panel. Figures 3 and 4 show that the panels do not influence each other when the distance is large. Both in-phase and out-of-phase they have the same frequency, which is equal to the eigenfrequency of the single panel in air (see the third row of Table (1)). This could be expected from the mathematical formulation (see Equation (31)).

For small gap width h the effects on the eigenvalues are completely different for in-phase vibration and out-of-phase vibration, as could be expected from Equations (35) and (37). The in-phase vibrating panels will feel only the air on one side of the panel. From Equation (35) it follows that the acoustic energy of two in-phase vibrating panels corresponds to the acoustic energy of a single solar panel with air on both sides, but with half the value of the density. As a consequence, the value of $\langle \mathcal{M}_a U_1, U_1 \rangle$ in (43) for two panels should converge to half the value for a single solar panel. According to (42) and (43), for small values of h, the frequencies of two in-phase vibrating panels should converge to the frequency of a single solar panel with air on both sides, but with half the value of its density. The first two eigenfrequencies of the latter problem have been calculated as 28·45 Hz and 63·45 Hz. Inspection of Figures 3 and 4 reveals that the eigenfrequencies of the in-phase vibrating panels converge correctly to these limit values.

For two out-of-phase vibrating panels (close to each other) the acoustic energy is inversely proportional to the distance h, as follows from Equation (37). As a consequence, the value of $\langle \mathcal{M}_a U_1, U_1 \rangle$ for two out-of-phase panels tends to ∞ as h tends to zero. As follows from (43), for small values of h, the eigenfrequencies of two out-of-phase vibrating panels should converge to zero. This is confirmed by the results of Figure 3.

3. Radar-Cross-Section (RCS) calculations

RCS predictions of aerospace platforms are essential to assess their visibility under radar surveillance. This requires the calculation of the electromagnetic field scattered by the platform when illuminated by a plane electromagnetic wave (the incident radar beam). For a large range of illumination angles the scattered field is governed by reflections from the external surface and by diffraction from sharp edges, such as the leading or trailing edge of the wing. To a certain extent, this field can be determined by approximate high-frequency methods based on physical and geometrical optics (see [12]). For nose-on illumination, however, the scattered field is dominated by multiple reflections from the interior surface of the engine inlet, which is a re-entrant cavity. The compressor stage of the inlet blocks the waves and reflects them back. The number of reflections inside the inlet depends strongly on the angle under which the beam enters, and on the geometry of the inlet. It will be shown that the scattered field from

the inlet results in a large, broad RCS lobe. The interactions between the multiply reflected waves require the application of more sophisticated methods (solving the Maxwell equations). In the present paper the applicability of boundary-integral-equation methods is discussed. The interior surface of the engine inlets is modelled as a three-dimensional perfectly conducting cavity-like screen.

3.1. Mathematical formulation

The electromagnetic fields satisfy the Maxwell equations and appropriate boundary conditions. For RCS calculations the electromagnetic field scattered by the object has to be determined, due to a plane wave (with direction vector $\mathbf{k}^i$) illuminating the object. With the incident plane wave an electric field is associated with direction $\mathbf{e}^i$ and magnitude E_0. The incident electric and magnetic fields are specified as:

$$\mathbf{E}^i = \mathbf{e}^i E_0 \, \mathrm{e}^{-jk\mathbf{k}^i \cdot \mathbf{r}}, \qquad \mathbf{H}^i = \sqrt{\epsilon/\mu}\, \mathbf{k}^i \times \mathbf{E}^i. \tag{44}$$

The total electromagnetic field in the domain outside the scattering object is written as the sum of the incident field and the scattered field,

$$\mathbf{E}^T = \mathbf{E}^i + \mathbf{E}^s, \qquad \mathbf{H}^T = \mathbf{H}^i + \mathbf{H}^s. \tag{45}$$

In a homogeneous source-free region the scattered field around a metallic object (*i.e.* a perfect electric conductor), with boundary S, can be represented by the Stratton-Chu boundary-integral formulas ([13], pp. 464–467) in terms of the electric surface current $\mathbf{J}$. The formula for the scattered electric field $\mathbf{E}^s$ reads

$$\mathbf{E}^s(\mathbf{r}) = \int_S \left\{ -j\omega\mu \mathbf{J} G - \frac{1}{j\omega\epsilon} (\nabla \cdot \mathbf{J}) \nabla G \right\} \mathrm{d}S, \quad \forall \mathbf{r} \notin S. \tag{46}$$

For the scattered magnetic field $\mathbf{H}^s$ holds

$$\mathbf{H}^s(\mathbf{r}) = \int_S \mathbf{J} \times \nabla G \, \mathrm{d}S, \quad \forall \mathbf{r} \notin S. \tag{47}$$

Here, ω the angular frequency of the electromagnetic field, μ the permeability of the free space ($\mu = 4\pi 10^{-7}$) and ϵ the permittivity of the free space ($\epsilon = 10^{-9}/36\pi$). The Green function G represents the fundamental solution of the Helmholtz equation (see Equation (7)). The wave number k in (7) is given by $k = \omega\sqrt{\epsilon\mu} = 2\pi/\lambda$, with λ the wavelength of the incident field. The integral formulations (46) and (47) can be derived from the vector Helmholtz equations when a vector equivalent of Green's second identity is used and the property that the total field is zero inside S (see *e.g.* [14], pp. 130–132). The vector operations in (46) and (47) are to be performed in source coordinates.

The electric surface current $\mathbf{J}$ in Equations (46) and (47) is equal to the tangential component of the total magnetic surface field over S,

$$\mathbf{J} = \mathbf{n} \times \mathbf{H}^T, \tag{48}$$

with $\mathbf{n}$ the outward normal to S.

For the special case of a perfect electrically conducting object, the tangential components of the total electric surface field are zero,

$$\mathbf{n} \times \mathbf{E}^T = 0. \tag{49}$$

Substitution of (45) and (46) in the boundary condition (49) yields the Electric-Field Integral Equation (EFIE)

$$\mathbf{n} \times \int_S \left\{ j\omega\mu \mathbf{J} G + \frac{1}{j\omega\epsilon} (\nabla \cdot \mathbf{J}) \nabla G \right\} \, \mathrm{d}S = \mathbf{n} \times \mathbf{E}^i. \tag{50}$$

The Magnetic-Field Integral Equation (MFIE) follows from Equations (45), (47) and (48),

$$\mathbf{J} = \mathbf{n} \times \mathbf{H}^T = \mathbf{n} \times \mathbf{H}^i + \mathbf{n} \times \int_S \mathbf{J} \times \nabla G \, \mathrm{d}S + \tfrac{1}{2}\mathbf{J}. \tag{51}$$

The last term in (51) follows from the jump relations of classical potential theory. This equation subsequently reduces to

$$\tfrac{1}{2}\mathbf{J} - \mathbf{n} \times \int_S \mathbf{J} \times \nabla G \, \mathrm{d}S = \mathbf{n} \times \mathbf{H}^i. \tag{52}$$

This is the general form of the MFIE, which is valid only for closed surfaces. For screens the EFIE has to be used. Since engine inlets of fighter aircraft are usually geometrically modelled as cavity-like screens, computational tools are being developed for the numerical solution of (50) in terms of a weak formulation. Multiply (50) by a tangential test function $\mathbf{W}$. Then, the following weak formulation can be derived: find the complex surface current vector $\mathbf{J} \in \tilde{H}_{\mathrm{div}}^{-1/2}(S)$, with the solution space as presented in [5], such that

$$\frac{j}{\omega\epsilon} \int_S \int_S \{k^2 \mathbf{J}.\mathbf{W}' \, G - (\mathrm{div}\mathbf{J})(\mathrm{div}'\mathbf{W}') \, G\} \, \mathrm{d}S' \, \mathrm{d}S = \int_S \mathbf{E}^i.\mathbf{W}' \, \mathrm{d}S, \tag{53}$$

for all $\mathbf{W}' \in \tilde{H}_{\mathrm{div}}^{-1/2}(S)$. Equation (53) describes the behaviour of the surface current on the object surface, as induced by the incident electromagnetic field $\mathbf{E}^i$. Once a solution of (53) has been found, the scattered electric field can be determined by applying the Stratton-Chu representation formula (46), or its far field asymptotic approximation.

When the object S represents a screen, it contains a boundary edge, which is denoted by ∂S. Let $\boldsymbol{\nu}$ be the unit normal along ∂S, in the tangent plane to S. Along ∂S the normal component $\boldsymbol{\nu} \cdot \mathbf{J}$ may not jump. Hence, for screens it is required that

$$\boldsymbol{\nu} \cdot \mathbf{J} = 0, \quad \text{along } \partial S. \tag{54}$$

Mathematical aspects, such as existence, uniqueness and regularity of solutions, of (53) for screen problems have been discussed in [15].

In Section 3.3 the accuracy of the numerical solutions of (53) is assessed. There, the results of (53) are compared with the results of two-dimensional models. To this end, consider a scatter problem in two-dimensional space for the case where the object has no variation in z-direction. Let Γ be the two-dimensional cross-section boundary of the object. Then the

Electric-Field Integral Equation (53) can be reduced to two independent scalar equations: one for Transverse Magnetic (TM^z) polarization (where the direction of the incident electric field $\mathbf{E}^i$ is aligned with the z-axis), and one for Transverse Electric (TE^z) polarization (where the direction of the incident magnetic field $\mathbf{H}^i$ is aligned with the z-axis).

For TM^z polarization the weak formulation reads: find the current $J \in H^{-1/2}(\Gamma)$ such that

$$\frac{\omega\mu}{4}\int_\Gamma\int_\Gamma \psi(\boldsymbol{\rho})J(\boldsymbol{\rho}\,')H_0^{(2)}(k \mid \boldsymbol{\rho}-\boldsymbol{\rho}\,' \mid)\,\mathrm{d}\Gamma'\,\mathrm{d}\Gamma = \int_\Gamma E_z^i(\boldsymbol{\rho})\psi(\boldsymbol{\rho})\,\mathrm{d}\Gamma, \tag{55}$$

for all $\psi \in H^{-1/2}(\Gamma)$. For TE^z polarization the weak formulation reads: find $J \in H_0^{1/2}(\Gamma)$ such that

$$\frac{1}{4\omega\epsilon}\int_\Gamma\int_\Gamma \left\{k^2(\mathbf{c}(\boldsymbol{\rho}).\mathbf{c}(\boldsymbol{\rho}\,'))\psi(\boldsymbol{\rho})J(\boldsymbol{\rho}\,') - \frac{\mathrm{d}\psi(\boldsymbol{\rho})}{\mathrm{d}c}\frac{\mathrm{d}J(\boldsymbol{\rho}\,')}{\mathrm{d}c}\right\}$$
$$H_0^{(2)}(k \mid \boldsymbol{\rho}-\boldsymbol{\rho}\,' \mid)\,\mathrm{d}\Gamma'\,\mathrm{d}\Gamma = \int_\Gamma E_c^i(\boldsymbol{\rho})\psi(\boldsymbol{\rho})\,\mathrm{d}\Gamma, \tag{56}$$

for all $\psi \in H_0^{1/2}(\Gamma)$. Here $H_0^{(2)}$ the Hankel-function of the second kind, $\mathbf{c}$ the unit tangential vector along the boundary Γ, $\boldsymbol{\rho}$ a point on the boundary Γ, E_z^i the z-component of the incident electric field, and E_c^i the tangential component of the incident electric field.

When the boundary Γ is not closed, the electric current J in Equation (56) has to vanish at the end-points of the boundary. This criterion corresponds to requirement (54) for screens in three-dimensional space.

3.2. Numerical solution

The surface current $\mathbf{J}$ in Equation (53) is approximated by

$$\mathbf{J} = \Sigma_n I_n \mathbf{J}_n, \tag{57}$$

where I_n are constants to be determined. The basis functions $\mathbf{J}_n$ are defined by the classical Glisson-Rao vector functions on a triangular surface grid (see [16]). Insert the representation (57) into the EFIE (53) and take the test functions equal to the basis functions. Then, a system of linear equations is obtained of the form $ZI = V$. The elements of the impedance matrix Z are given explicitly by

$$Z_{mn} = \frac{j}{\omega\epsilon}\int_S\int_S \{k^2\mathbf{J}_m\cdot\mathbf{J}_n'\,G - (\mathrm{div}\mathbf{J}_m)(\mathrm{div}'\mathbf{J}_n')\,G\}\,\mathrm{d}S'\,\mathrm{d}S, \quad \forall(m,n). \tag{58}$$

The Glisson-Rao basis functions were selected because of their applicability to a general class of geometries and for reasons of accuracy and efficiency (see also [16]). These basis functions have local support on a pair of triangles sharing a common edge, so that the inner (respectively outer) integration on the right-hand side of expression (58) is restricted to the support of $\mathbf{J}_n'$ (respectively $\mathbf{J}_m$) only. Thus, the double integral in (58) involves at most four triangles. Different types of quadrature rules are applied to calculate (58), depending on the required integration accuracy. The Glisson-Rao basis functions have a continuous normal

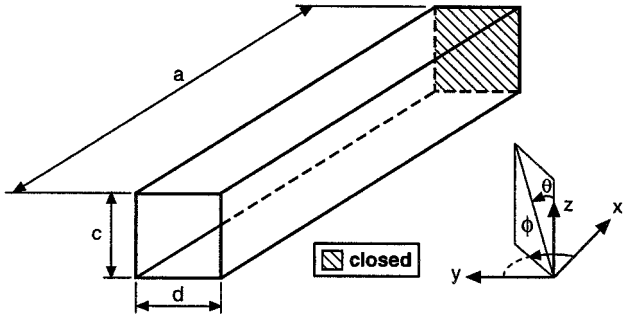

Figure 5. Rectangular inlet with length $a = 10\lambda$, width $d = 2\lambda$, heigth $c = 2\lambda$.

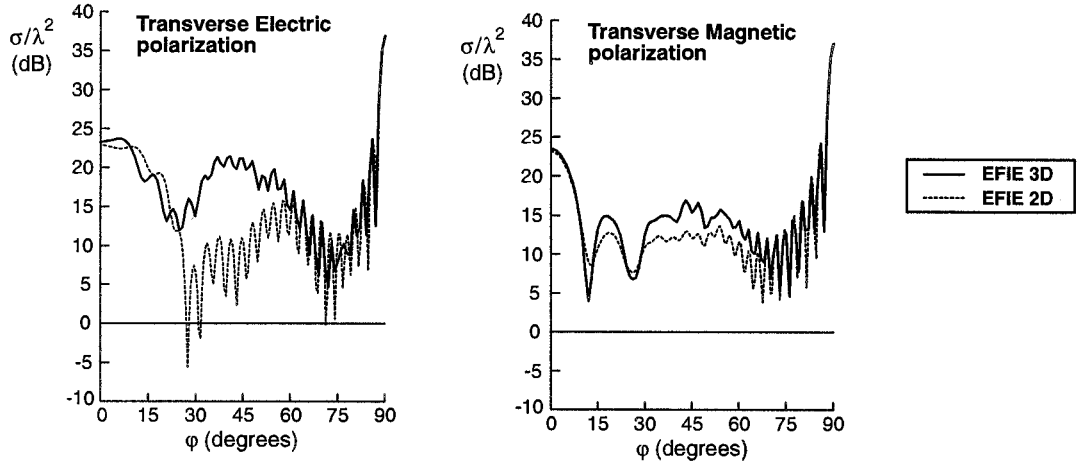

Figure 6. Comparison of RCS calculations for rectangular inlet in Figure 5.

component when crossing the common edge. The unknowns I_n in (57) are attached to common edges. When the scattering object defines a screen, edges of triangular patches have no neighbouring counterpart along the boundary ∂S. At these edges $I_n = 0$ according to (54). The computational model based on the above approach is called EFIE3D.

The two-dimensional electric field integral equations (55) and (56) have been solved numerically by means of a boundary-element Galerkin method. The boundary Γ of the object is partitioned into a number of segments and the electric currents are approximated by local functions on the boundary. In Equation (55) the basis and test functions are taken piecewise constant, whereas they are taken piecewise linear in Equation (56). This numerical approach has resulted in the EFIE2D computational model.

3.3. Accuracy of RCS predictions

The RCS of an object is defined as $\sigma = \lim_{r\to\infty} 4\pi r^2 |\mathbf{E}^s|^2/|\mathbf{E}^i|^2$, where r is the distance from object to observer. The dimension of σ is area, usually in square meters, or it may be nondimensionalized by division of the wavelength squared, σ/λ^2. When the transmitter and receiver are at the same location, the RCS is usually referred to as monostatic. It is referred to as bistatic when the two are at different locations.

In order to assess the accuracy of the RCS predictions the EFIE3D model has been applied to a rectangular inlet with length 10λ, width 2λ and height 2λ. The geometry of this inlet is

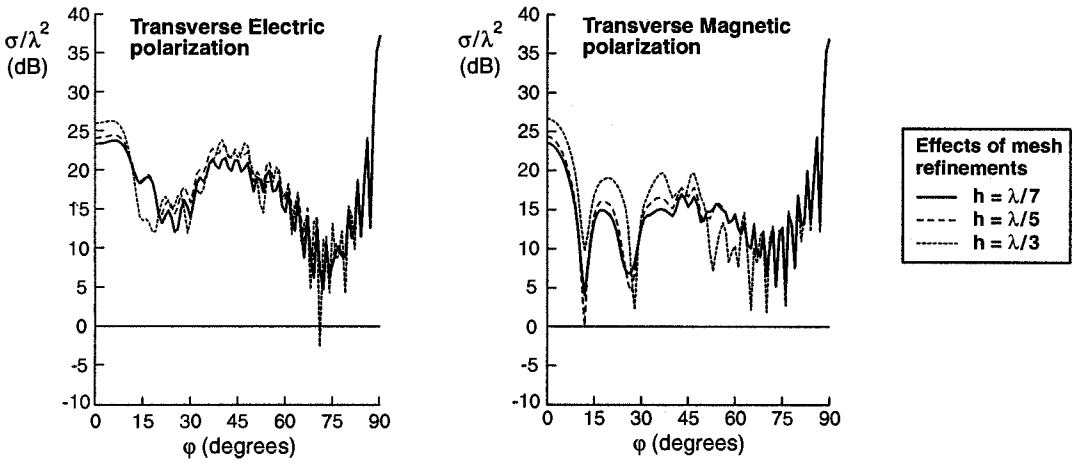

Figure 7. Assessment of accuracy of RCS calculations for rectangular inlet in Figure 5.

shown in Figure 5. The calculations have been carried out on uniform triangular surface grids which are planar symmetric about the planes $y = 0$ and $z = 0$. The surface grids are obtained as follows. First, a uniform rectangular grid is generated with mesh-size h. Subsequently, each quadrilateral element is divided into two triangular elements.

The accuracy of the computed RCS is assessed in two ways:

(i) by a comparison of the RCS results with the results of the EFIE2D model for an infinite rectangular inlet (cross section $10\lambda \times 2\lambda$ extending from $z = -\infty$ to $z = +\infty$, and
(ii) by refinement of the grid.

In Figure 6 the RCS predictions of the EFIE3D model are compared with the predictions of the EFIE2D model. The 3D calculations have been carried out on the uniform triangular grid with a characteristic meshsize of $h = \lambda/7$. It is observed that the three-dimensional results show the same scattering characteristics as do the two dimensional results. For TM^z-polarization the scattering of the 3D inlet and the 2D inlet are expected to agree because the direction of the incident electric field is parallel to the z-axis. Therefore the horizontal plates of the 3D inlet will not contribute to the RCS, because the right-hand side of (50) vanishes at these plates. This is confirmed by Figure 6, although in the interval between $\phi = 10°$ and $\phi = 60°$ the RCS of EFIE 3D is slightly higher, due to the rather coarse sampling that has been used in the EFIE3D model. For TE^z-polarization the higher values of the 3D RCS predictions in this interval are mainly due to the contributions of the horizontal plates of the 3D inlet which are not present in the 2D computations.

The convergence of the 3D RCS predictions is assessed in Figure 7, where results are presented of EFIE3D calculations on uniformly triangular discretizations with meshsizes of $h = \lambda/3$, $h = \lambda/5$ and $h = \lambda/7$, respectively. This figure apparently reveals that the triangular discretization with meshsize $h = \lambda/3$ is too coarse to get an accurate RCS prediction at the open side of the inlet. The RCS predictions of the EFIE3D model improve when the mesh is refined. For a discretization with meshsize $h = \lambda/7$ reliable RCS results are obtained.

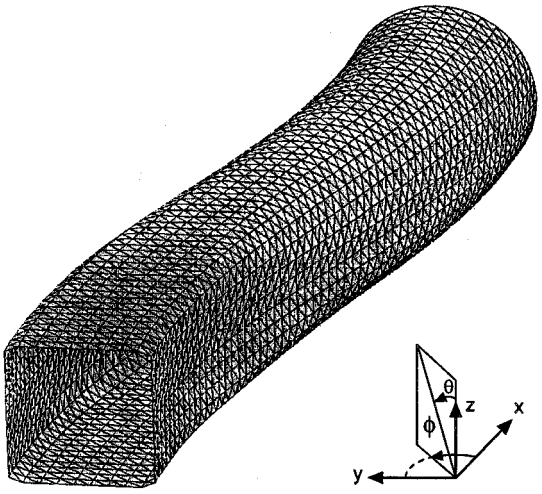

Figure 8. Computational surface grid of a curved engine inlet with square entrance (4454 panels) at a frequency of 1.5 GHz; the length of the inlet is about 4 meter.

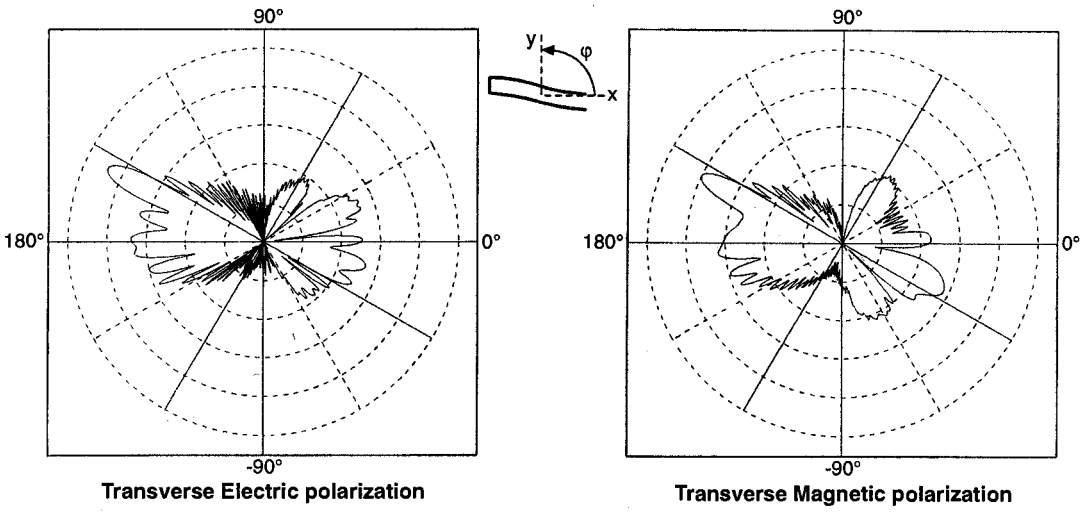

Figure 9. Calculated bistatic RCS of a curved inlet for an illumination angle $\phi = -25°$, $\theta = 90°$, and radar frequency 1.5 GHz.

3.4. Application to an engine inlet

The EFIE3D model has been applied to analyse the RCS of a curved engine inlet with a square entrance (Figure 8). It has a curved axis of 4 meters length. The surface has been approximated by 4454 triangular patches (Figure 8). The coordinate system (see Figure 8) has been chosen such that the inlet is illuminated on the open side at $\phi = 0°, \theta = 90°$. At a frequency of 1·5 GHz (wavelength 20 cm) and an illumination angle of $\phi = -25°, \theta = 90°$, the scattered electric field has been computed. In Figure 9 the bistatic RCS characteristics are displayed with the observer in the $xy-$ plane (*i.e.* $\theta = 90°$). The maximum around $\phi = 155°$ (the 'forward lobe') arises from the scattered electric field compensating for the incident field. The peak near $\phi = -165°$ is due to single reflection of the incident waves. The bistatic cross section is rather small in the vicinity of $-90°$ or $+90°$ as the receiver direction is perpendicular

to the direction of the incident field. Thus, the shape of the inlet is such that there is hardly any scattering in these directions. Most of the scattering in this scattering range is due to diffraction on the sharp edges at the top and bottom of the inlet entrance. In the neighbourhood of $\phi = 0^\circ$ the scattering cross section has a smoother behaviour due to the fact that waves coming out of the inlet have multiply reflected inside. The local maximum in the vicinity of $\phi = \pm 25^\circ$ is caused mainly by multiple reflections at the inlet wall and the inlet face. From this observation point the inlet face and the local maxima of the surface current can be 'seen'.

3.5. Applicability of boundary-integral equation methods

The applicability of the computational model as described in Section 3.2 is frequency limited because of the numerical approach involved in the model and due to computer hardware limitations. On the currently available supercomputers the model can be applied to engine inlets of fighter aircraft up to radar frequencies of about 1 GHz. For higher frequencies the computation times become too large and the computer storage required is not available. Therefore, many research efforts are aimed at increasing the applicability of boundary-integral-equation methods to higher frequencies. A promising approach appears to be the application of entire-domain functions (see *e.g.* [17]). These functions have global support instead of local support on triangular patches. It is foreseen that the dimension of the impedance matrix will then decrease, so that the integral-equation methods will become applicable to higher frequencies. Similar entire-domain functions were used by Multhopp [1] in the 1950's to predict the lift distribution on wings in the subsonic speed regime. The use of these functions was advantageous from the point of view that a small system of equations results, which could be solved by the computational means available at that time. The mathematical formulation of entire-domain functions requires that the surface can be mapped onto a simple rectangular computational domain. Therefore, geometries like engine inlets have to be decomposed into subdomains, in such a way that each part can be represented by a continuous mapping; *e.g.* the surface of the engine inlet of Figure 8 has to be decomposed into two parts, one part describing the circumferential boundary and a second part describing the rear face. Then, at each part appropriate entire-domain functions are defined. Along the common edges of the subdomains the entire-domain functions have to match. In general, this is a difficult task. Therefore, it is recommended to apply the classical Glisson-Rao basis functions (with local support) only in the neighbourhood of the edges, and to apply the entire-domain functions elsewhere. This approach involves the specification of so-called cut-off functions that define the region where the local basis functions are used. At the National Aerospace Laboratory NLR the applicability of this approach is being investigated for the numerical solution of the two-dimensional electric-field integral equations (55) and (56). It appears that the computation of the coefficients of the impedance matrix requires the numerical calculation of integrals with strongly oscillating integrands. Integration techniques such as those developed in the 1960's (*e.g.* [18]) are essential to decrease the computational costs for the calculation of the impedance matrix.

An alternative approach to increase the applicability of boundary-integral-equation methods to higher frequencies is the development of parallel algorithms for the solution of (53) and the implementation on parallel hardware architectures (see *e.g.* [19]).

4. Concluding remarks

In the present paper two problems in aerospace research have been addressed which involve the numerical solution of boundary-integral equations on screens. The first problem is concerned with the structural-acoustic analysis of light-weight solar array panels, which are geometrically modelled as screens. The second problem is related to RCS predictions of engine inlets of fighter aircraft, where the interior surface of the engine inlet is modelled as a perfectly conducting cavity-like screen.

The acoustic effects of the surrounding air on the dynamic behaviour of solar arrays have been analysed for two cases: a single solar panel and an array consisting of two parallel solar panels in close proximity. For low frequencies, the single solar panel experiences the air as an added virtual mass. As a consequence, the computed eigenfrequencies are shifted downwards significantly. For two parallel panels, estimates for the acoustic energy of the vibrating air have been derived in terms of the small distance h between the two panels. For h tending to zero, the acoustic energy of two in-phase vibrating panels tends to half the value for two single solar panels (without interaction). For two out-of-phase vibrating panels the acoustic energy is inversely proportional to the distance h, when h tends to zero. Inspection of the computed eigenfrequencies has confirmed that the behaviour of the lowest eigenfrequencies is consistent with these energy estimates for small values of h.

RCS predictions of engine inlets of fighter aircraft are obtained by a boundary-integral-equation method for the solution of the electric-field integral equation. The accuracy of RCS predictions has been assessed for a rectangular inlet with length 10λ, width 2λ and height 2λ. From the results of Section 3.3 it is obvious that multiple reflections inside engine inlets can be accurately modelled provided that surface grids are used with at least seven patches per wavelength in one direction (*i.e.* $h = \lambda/7$). The boundary-integral-equation method has been applied to analyse the RCS of a curved engine inlet with a square entrance. At the open side the computed RCS shows broad smooth lobes, which are caused by multiple reflections at the inside wall of the inlet.

The numerical methods to solve the boundary-integral equations of the above problems use local basis functions on triangular surface grids. They require the generation of a complex-valued matrix. The dimension N of this matrix is proportional to the square of the frequency. The computational cost for solving the equations is proportional to N^3. For objects which are large with respect to the wavelength, the numerical methods using these local basis functions can become intractable, because the computational resources required are not available. In particular, for RCS calculations the described boundary-integral methods can only be applied to engine inlets of fighter aircraft up to radar frequencies of about 1 GHz on the currently available supercomputers. Many research investigations are going on, worldwide, to increase the applicability of boundary-integral-equation methods to higher frequencies. Instead of using local basis functions, there is renewed interest in the application of appropriate basis functions with global support, which were also used to solve boundary-integral equations before digital computers became available. The aim of these investigations is to decrease the dimension of the matrix of influence coefficients and to lower the computer storage required.

Acknowledgements

Some parts of this investigation were supported by the Netherlands Ministry of Defense and

monitored by the Scientific Support Division of the Directorate of Material Royal Netherlands Airforce. Other parts were supported by the Netherlands Agency for Aerospace Programs (NIVR). The EFIE3D computational model was developed in a cooperative programme with DASA-MA (Munich).

The author would like to thank his colleagues F. P. Grooteman and F. Klinker for carrying out parts of the calculations. The author is grateful to J. van der Vooren for his valuable advice in preparing this paper.

References

1. H. Multhopp, *Methods for Calculating the Lift Distribution of Wings (Subsonic Lifting Surface Theory)*. Report no. Aero 2353 R.A.E. (1950) 97pp.
2. P. J. Zandbergen, T. E. Labrujere and J. G. Wouters, *A new Approach to the Numerical Solution of the Equation of Subsonic Lifting Surface Theory*. NLR TR G.49, National Aerospace Laboratory NLR (1967) 31pp.
3. T. E. Labrujere and P. J. Zandbergen, On the application of a new version of lifting surface theory to non slender and kinked wings, *J. of Eng. Math.* 7 (1973) 85–96.
4. K. M. Liew, K. C. Hung and M. K. Lim, Vibration of Mindlin plates using boundary characteristic orthogonal polynomials. *J. of Sound and Vibr.* 182 (1995) 77–90.
5. E. P. Stephan, Boundary integral equations for screens in $\mathbf{R}^3$. *Integral Equations and Operator Theory* 10 (1987) 236–257.
6. F. P. Grooteman and H. Schippers, *Coupled Analysis in Acoustics on the Dynamical Behaviour of Solar Arrays*. NLR TP 94268, National Aerospace Laboratory NLR (1994) 17pp.
7. J. C. Nedelec, Approximation par potential de double conche du problème de Neumann Exterieur, *C.R. Acad. Sci. Paris, Ser. A* 286 (1977) 616–619.
8. H. T. Koelink, H. Schippers, J. J. Heijstek and J. J. Derksen, *Modal Analysis of Solar Panels Using Boundary Integral Equations*. NLR TP 92281, National Aerospace Laboratory NLR (1992) 13pp.
9. H. Schippers and J. J. Heijstek, *Modal Analysis of Solar Arrays Using Hypersingular Integral Equations*, NLR TP 91267, National Aerospace Laboratory NLR (1991) 15pp.
10. W. M. Beltman, P. J. M. van der Hoogt, R.M.E.J. Spiering and H. Tijdeman, Air loads on solar panels during launch. In: European Space Agency (org.), *Proceedings of the Conference on Spacecraft Structures Materials and Mechanical Testing*, ESA SP-386. Noordwijk: ESA (1996) pp. 219–226.
11. K. C. Park and D. L. Flaggs, A symbolic Fourier Synthesis of a one-point integrated quadrilateral plate element. *Comp. Meth. Appl. Mech. Engr.* 48 (1985) 203–236.
12. H. Schippers, M. G. E. Brand, J. E. J. Maseland and J.J. Heijstek, *On the Radar Cross Section Prediction of Aerospace Platforms*. NLR TP 94486, National Aerospace Laboratory NLR (1994) 20pp.
13. J. A. Stratton, *Electromagnetic Theory*. New York: McGraw-Hill (1941) 615pp.
14. S. Silver, *Microwave Antenne Theory and Design*. London: Peter Peregrinus (1984) 623pp.
15. T. Abboud and F. Starling, Scattering of an Electromagnetic wave by a Screen. In: M. Costabel, M. Dauge and S. Nicaise (eds.) *Boundary Value Problems and Integral Equations in Nonsmooth Domains*. Lecture Notes in Pure and Applied Mathematics, 167. New York, Basel, Hong Kong: Marcel Dekker, Inc. (1995) pp. 1–17.
16. S. M. Rao and D. R. Wilton and A.W. Glisson, Electromagnetic Scattering by Surfaces of Arbitrary Shape. *IEEE Trans. Ant. Prop.* AP-30 (1982) 409–418.
17. D. S. Wang, Current-Based Hybrid Analysis for Surface-Wave Effects on Large Scatterers. *IEEE Trans. Ant. Prop.* AP-39 (1991) 839–850.
18. A. I. van de Vooren and H.J. van Linde, Numerical calculation of integrals with strongly oscillating integrand. *Math. Comp.* 20 (1966) 232–245.
19. F. Choukroun, *Solveur direct parallèle en acoustique and électromagnétisme, pour les obstacles 3D axi-symmétriques. Problémes á hautes fréquences.* Onera N.T. 1997–5, Onera, Châtillon, France (1997) 233pp.